# Three-dimensional tomography of the 1992 southern California earthquake sequence: Constraints on dynamic earthquake rupture?

SPECIAL REPORT

Jonathan M. Lees Department of Geology and Geophysics, Yale University, New Haven, Connecticut 06511
Craig Nicholson Institute for Crustal Studies, University of California, Santa Barbara, California 93106

## ABSTRACT

**Tomographic inversion of *P*-wave arrival times from aftershocks of 1992 southern California earthquakes is used to produce three-dimensional images of subsurface velocity. The preliminary 1992 data set, augmented by the 1986 M 5.9 North Palm Springs sequence, consists of 6458 high-quality events recorded by the permanent regional network—providing 76 306 raypaths for inversion. The target area consisted of a 104 × 104 × 32 km$^3$ volume divided into 52 × 52 × 10 rectilinear blocks. Significant velocity perturbations appear to correlate with rupture properties of recent major earthquakes. Preliminary results indicate that a low-velocity anomaly separates the dynamic rupture of the M 6.5 Big Bear event from the M 7.4 Landers main shock; a similar low-velocity region separates the M 6.1 Joshua Tree sequence from the Landers rupture. High-velocity anomalies occur at or near nucleation sites of all four recent main shocks (North Palm Springs–Joshua Tree–Landers–Big Bear). A high-velocity anomaly is present along the San Andreas fault between 5 and 12 km depth through San Gorgonio Pass; this high-velocity area may define an asperity where stress is concentrated and where future large earthquakes may begin.**

## INTRODUCTION

The 1992 southern California earthquake sequence began in April with the M 6.1 Joshua Tree earthquake and culminated with the aftershocks of the June 28 M 7.4 Landers and M 6.5 Big Bear events. These earthquakes represent the most extensive and well-recorded sequence of seismicity in the history of southern California (Hauksson et al., 1992). The Joshua Tree event produced right slip along 10–15 km of the north-trending West Deception Canyon fault (Nicholson and Hauksson, 1992; Rymer, 1992) in the Little San Bernardino Mountains east of the San Andreas fault (Fig. 1); it was followed by more than 6000 (M > 1) aftershocks. The Landers main shock ruptured unilaterally to the north and then northwest along the Johnson Valley, Homestead Valley, Emerson, and Camp Rock faults (Fig. 1); an average of 3–5 m of right slip was produced over nearly 70 km. The Big Bear event occurred in the San Bernardino Mountains (Fig. 1) and involved left slip along 40 km of a northeast-trending fault (Hauksson et al., 1992). The Landers–Big Bear sequence included more than 15 000 (M > 1) aftershocks within the first three months. The extensive arrival-time data from these earthquakes provide a unique opportunity to analyze the subsurface velocity structure and to resolve the relations among structure, tectonics, and major earthquakes in an area adjacent to a critical section of the southern San Andreas fault.

## DATA SELECTION AND ANALYSIS

The data selected for this preliminary study include aftershocks from the 1986 North Palm Springs earthquake and from the recent major events of April and June 1992 in southern California. The North Palm Springs sequence was used previously in a tomographic inversion for three-dimensional (3D) velocity structure in the northern Coachella Valley (Nicholson and Lees, 1992). The only events used had ten or more *P*-wave arrivals at 56 stations located within the target area (Fig. 1). The data consisted mostly of recordings at permanent network stations operated by Caltech and the U.S. Geological Survey, but data from the 1986 North Palm Springs portable deployment were also included. Events for which locations were not well determined were ex-

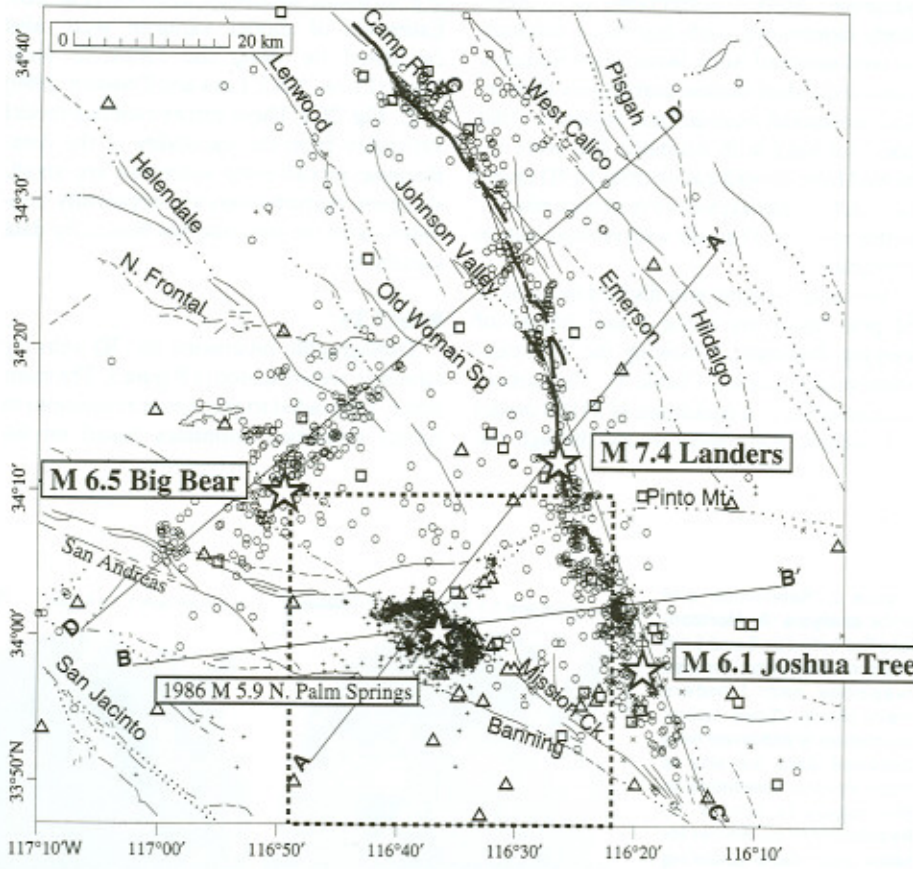


**Figure 1. Map of target area for velocity inversion, 1992 southern California earthquake sequence, showing major faults and epicenters used in inversion. Dashed-line box is target area of previous inversion (Nicholson and Lees, 1992). Triangles represent permanent stations of regional network (plus stations deployed in 1986); squares are portable stations deployed in 1992 and not used in this analysis. Stars mark four main-shock epicenters. Cross-section orientations for Figure 4 are shown for reference.**

TABLE 1. LANDERS REFERENCE MODEL

| Layer | Depth to top (km) | Ref. vel. (km/s) | Slowness (%) min. | Slowness (%) max. | Velocity (km/s) min. | Velocity (km/s) max. |
|---|---|---|---|---|---|---|
| 1 | 0.00 | 3.40 | -6.82 | 7.94 | 3.15 | 3.65 |
| 2 | 1.60 | 4.80 | -2.03 | 3.42 | 4.64 | 4.90 |
| 3 | 2.00 | 5.50 | -5.03 | 15.31 | 4.77 | 5.79 |
| 4 | 3.10 | 5.80 | -7.58 | 8.18 | 5.36 | 6.28 |
| 5 | 5.50 | 6.20 | -2.91 | 4.43 | 5.94 | 6.39 |
| 6 | 8.00 | 6.30 | -3.14 | 4.38 | 6.04 | 6.50 |
| 7 | 12.00 | 6.45 | -3.65 | 5.67 | 6.10 | 6.69 |
| 8 | 16.00 | 6.70 | -3.79 | 3.08 | 6.50 | 6.96 |
| 9 | 23.00 | 7.20 | -0.36 | 1.49 | 7.09 | 7.23 |

cluded from the data set, as well as any unusually large traveltime residuals (i.e., >0.5 s), deemed outliers. Altogether, this left 6458 earthquakes with 76 306 raypaths for the inversion.

The tomographic inversion determines 3D velocity perturbations relative to an initial one-dimensional (1D) model (Lees and Crosson, 1989). For this inversion, the 1D reference model was taken from our earlier study (Nicholson and Lees, 1992) with only slight modifications (Table 1). This 1D model was checked against results from a joint hypocenter-velocity inversion. Because the 1D velocity perturbations were found to be small, the original model was assumed to be adequate. Station corrections were iteratively determined such that mean residuals at well-sampled sites were approximately zero. Individual station corrections thus reflect additional near-surface structure (that does not vary with azimuth) and were removed from consideration prior to 3D inversion. All earthquakes were relocated relative to this revised 1D model with revised station corrections.

The target volume was divided into a 52 × 52 grid region by using 2 km$^2$ blocks of varying thickness, following the 1D reference velocity model (Table 1). This procedure resulted in a maximum of 24 000 model parameters. Rays were traced through the 1D model, and perturbations of slowness were calculated within each block of the 3D model such that the sum of the squared traveltime residuals (observed minus predicted) is minimized in a single-step, first-order linear adjustment (Lees and Crosson, 1989). The data were weighted according to estimates of the original quality factors (0–3) provided with each phase reading. Effects of noisy data were reduced by constraining the Laplacian (second spatial derivative) of the slowness field to be small within horizontal layers, effectively smoothing the model laterally. The resulting system of simultaneous equations was solved by an iterative conjugate gradient technique (Lees and Crosson, 1989), and the sum of squared traveltime residuals was reduced by ~40% of its initial value.

Resolution was estimated by calculating impulse responses for different parts of the model (Lees and Crosson, 1989). Near the center of the model, where the ray coverage was most dense, the lateral and vertical resolution length was found to be slightly better than 4 km (2–4 blocks) (Fig. 2A), in contrast to farther north where smearing occurred in a northeast-southwest direction (Fig. 2B). Estimates of model variance were also calculated by using the Jackknife technique (Efron, 1982; Lees and Crosson, 1989) (e.g., Fig. 2C). These errors estimate model variability from the variability of the data. Because model error estimates are small, slowness perturbations are apparently consistent with the data and not biased by data variability.

## RESULTS

Tomographic inversions for 3D velocity structure are presented in Figure 3. The color scales are graded to gray (poor resolution) to reflect resolution estimates based on hit counts for each block. Lateral variations in layers 1 and 2 of the model are not well resolved, owing to the near-vertical incidence of the emerging rays, and are not presented.

The 3D tomographic results (Figs. 3 and 4) exhibit significant velocity perturbations that appear to correlate with various rupture properties of the four major recent earthquakes. Along the San Andreas fault in the North Palm Springs area, a high-velocity anomaly occurs between 5 and 12 km depth that corresponds to the region of maximum dynamic slip during the North Palm Springs main shock (Hartzell, 1989), as noted previously by Nicholson and Lees (1992). Between 5 and 12 km depth (layers 5 and 6, Fig. 3) are two high-velocity regions along the Landers main-shock rupture: one just north of the Landers hypocenter and another along the Camp Rock–Emerson fault farther north (Fig. 4C). These correspond to the locations of the two major Landers mainshock subevents, on the basis of long-period regional records (Campillo and Archuleta, 1992), and regions of high dynamic slip, as calculated from strong-motion records (Wald et al., 1992). In the Joshua Tree area, maximum dynamic slip appears to be localized along a velocity discontinuity separating a high-velocity region to the west from a low-velocity region to the east (layer 6, Fig. 3). Similarly, much of the Big Bear rupture appears to have been concentrated in an area of northeast-trending high-velocity anomalies (layer 5, Fig. 3; Fig. 4D). Thus, all four major earthquakes occurred in close proximity to high-velocity regions. A large, long, high-velocity anomaly is present along the San Andreas fault between 5 and 12 km depth through San Gorgonio Pass (layers 5 and 6, Fig. 3).

Correlations are also found between rupture termination points and regions of low

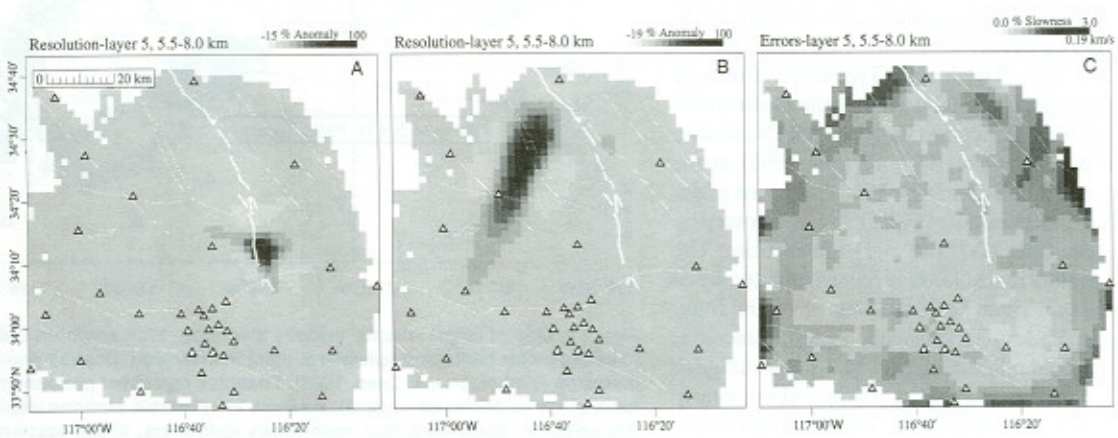


**Figure 2. Resolution and error analysis. A: Horizontal slice between 5 and 8 km depth of resolution impulse response near Landers main shock. Good lateral resolution is achieved here because data density is high. Vertical resolution in this region is similar. B: Resolution to northwest for same layer. Note smearing in the northeast-southwest direction; thus, the north-trending low-velocity anomaly observed in this region is not an artifact of smearing. C: Jackknife estimates of variance of slowness in layer 5 of model. Estimates in center of model are very low, indicating very consistent data set.**

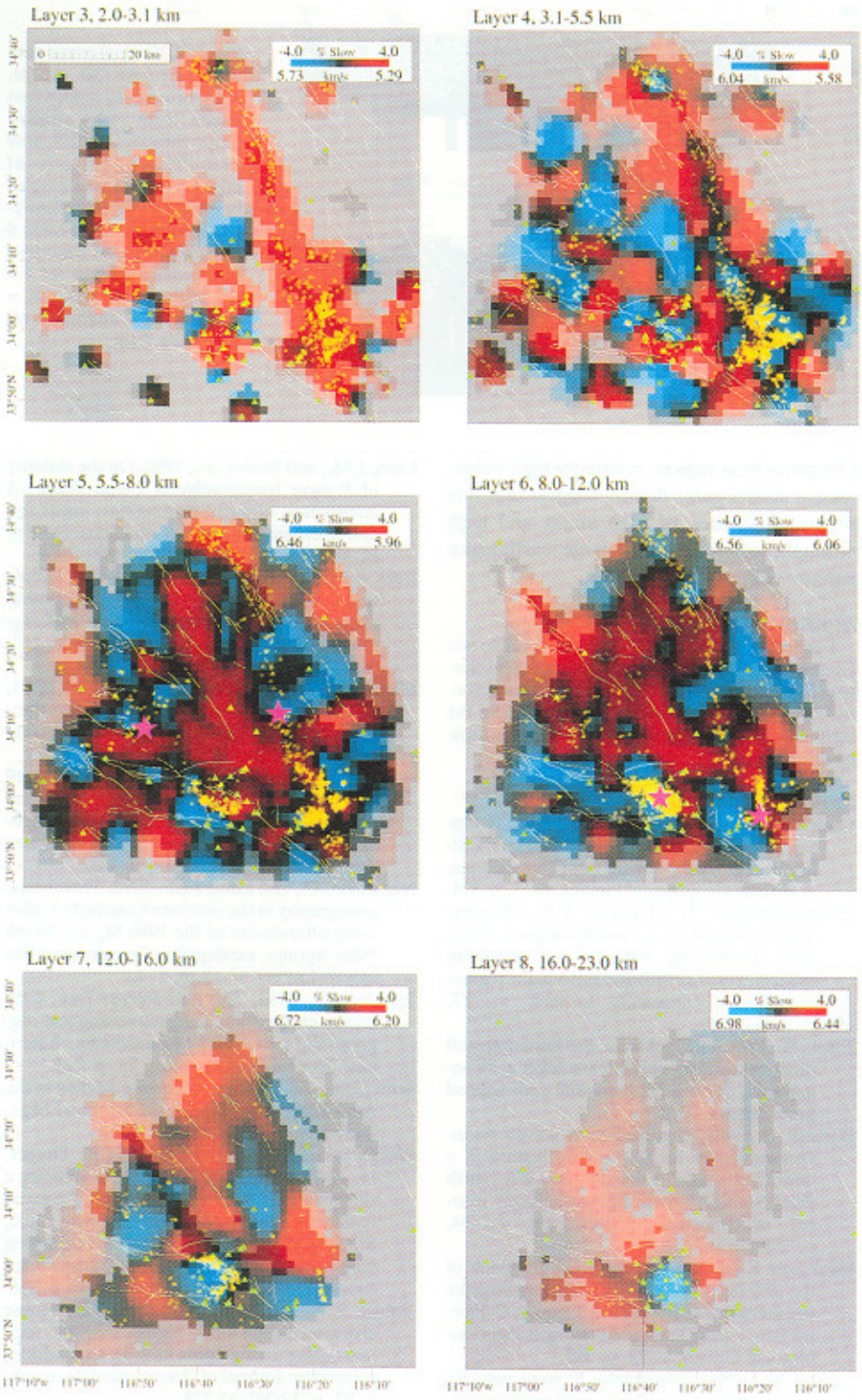


**Figure 3. Tomographic velocity-inversion results displayed as percent perturbations from reference 1D velocity model of Table 1. Plots vary from −4% (blue, high velocity) to +4% (red, low velocity) slowness perturbation; corresponding velocities are marked on each scale. Color scales shade to gray (less intensity) according to hit count of each block to convey where model is poorly resolved. Yellow circles are hypocenters of earthquakes within each layer; magenta stars represent main shocks in 1986 and 1992. White lines are mapped faults.**

velocity. A low-velocity anomaly parallels much of the Landers rupture to the west and dips to the west to 12 km depth (layers 5 and 6, Fig. 3). This low-velocity zone separates the dynamic rupture of the northeast-propagating M 6.5 Big Bear earthquake from that of the M 7.4 Landers sequence (Fig. 4D). A similar low-velocity zone is identified along the Pinto Mountain fault and separates the April M 6.1 Joshua Tree main shock from the June M 7.4 Landers event. Another low-velocity zone crosses the Landers rupture near the Homestead Valley fault segment, where dynamic slip during the main shock reached a minimum (Campillo and Archuleta, 1992; Wald et al., 1992). A low-velocity zone crosses the southern San Andreas fault at the point where the 1986 North Palm Springs rupture terminated to the south (layers 5 and 6, Fig. 3). Thus, locations of both high- and low-velocity anomalies appear to have affected the distribution of dynamic slip during recent major earthquakes.

## DISCUSSION

These observed correlations between velocity structure and earthquake behavior are not unique. Previous inversion studies have revealed similar correlations in other areas, particularly along other segments of the San Andreas fault (Lees and Malin, 1990; Michael and Eberhart-Phillips, 1991; Nicholson and Lees, 1992). At Parkfield, a correlation between high velocity and high background seismicity was observed, and the main-shock and foreshock region of the 1966 M 5.5 event was noted to have high velocity (Lees and Malin, 1990). At Loma Prieta, high-velocity anomalies along the San Andreas fault correlated with maximum dynamic slip during the 1989 M 7.1 earthquake (Eberhart-Phillips et al., 1990; Lees, 1990). These high-velocity areas were interpreted as representing stronger, more competent material, defining major asperities where stress is concentrated and large earthquakes tend to nucleate (Lees, 1990). The tomographic results presented here appear to agree with trends observed elsewhere along the San Andreas fault. Tomographic studies in the Anza region along the San Jacinto fault, by contrast, show no apparent correlation between areas of high seismicity and high velocity (Scott, 1992). We have no current explanation for this discrepancy. Perhaps apparent correlations between earthquakes and velocity anomalies observed at some locations along the San Andreas fault system are lithologic in origin.

One of the more intriguing observations, however, is the correlation between dynamic rupture termination points (or areas of minimum slip) and low-velocity areas along active faults. The low-velocity features appear to define weaker regions that cannot sustain high levels of stress or accumulated strain energy. These regions may be weaker because of material properties or variations in fracture density or possibly because of reduced local effective stress levels. In a detailed 3D seismic tomography exper-

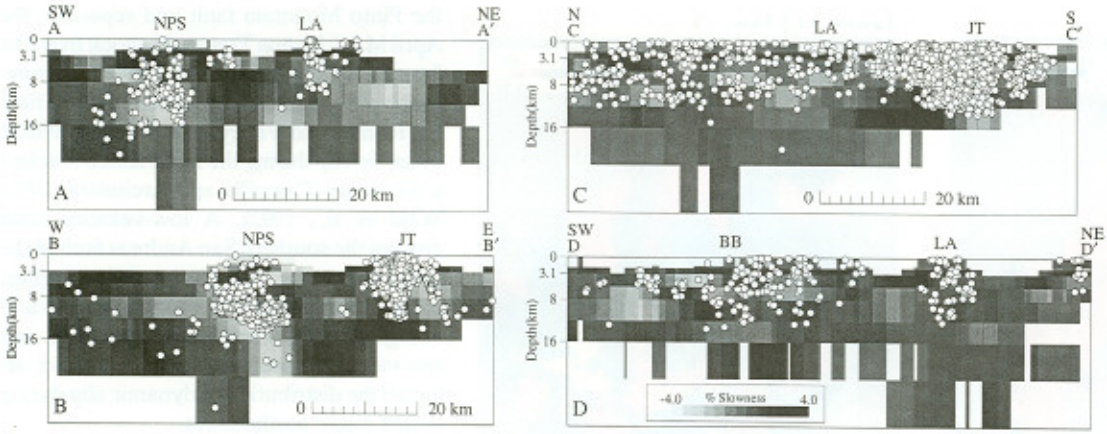


**Figure 4. Vertical cross sections through 3D model. Plots are in gray scales that grade from light shades (high velocity) to dark (low velocity). Locations of cross sections are plotted in Figure 1. Earthquake hypocenters (circles) within 5 km are projected onto vertical cross sections. NPS = North Palm Springs, LA = Landers, JT = Joshua Tree, BB = Big Bear.**

iment across the pillar of a deep, active gold mine, high velocities correlated with rock bursts, microseismicity, and areas of high stresses measured in situ, whereas low velocities were found in an area of low stress and little or no microearthquake activity (Young and Maxwell, 1992). The technique of tomographic velocity imaging may thus offer an effective means of segmenting active faults at depths, particularly in areas where previous attempts to segment faults based on surface geologic features have proved unreliable.

We view the results of our study as preliminary, although the gross features are most likely stable (Lees and Shalev, 1992). A more detailed analysis will include the extensive near-field data recorded by portable instruments deployed immediately following the 1992 main shocks (Fig. 1), and a full nonlinear, joint hypocenter-velocity inversion will be performed. Gravity constraints on the tomographic velocity inversion (Lees and Vandecar, 1991) will be included.

## SUMMARY AND CONCLUSIONS

Tomographic traveltime inversion for *P*-wave velocity structure in southern California, using aftershock sequences from 1986 and 1992, has revealed significant correlations between seismic activity and the behavior of major earthquake ruptures with variations in 3D velocity. We observed that regions of apparent high velocity along active faults typically exhibit the largest dynamic rupture. Dynamic ruptures also appear to terminate in areas of relatively lower velocity. This finding suggests that regions of low apparent seismic velocity are perhaps weaker and cannot sustain high levels of stress where large amounts of strain energy are concentrated, as compared with regions of high velocity, where maximum dynamic slip occurs and large ruptures tend to nucleate. Along the San Andreas fault, in the San Gorgonio Pass region, relatively high velocities at seismogenic depths suggest that this region is an area of high stress and high strength, where a future large earthquake rupture may nucleate.


## ACKNOWLEDGMENTS

Funded by grants from the Southern California Earthquake Center and the U.S. Geological Survey. We thank Donna Eberhart-Phillips for velocity information in advance of publication and the staff of the SCEC Data Center for providing high-quality data.


## REFERENCES CITED


Campillo, M., and Archuleta, R.J., 1992, A rupture model for the 28 June 1992 Landers, California, earthquake [abs.]: Eos (Transactions, American Geophysical Union), v. 73, p. 374.

Eberhart-Phillips, D., Labson, V.F., Stanley, W.D., Michael, A.J., and Rodriguez, B.D., 1990, Preliminary velocity and resistivity models of the Loma Prieta earthquake region: Geophysical Research Letters, v. 17, p. 1235–1238.

Efron, B., 1982, The Jackknife, the Bootstrap and other resampling plans: Philadelphia, Pennsylvania, Society for Industrial and Applied Mathematics, 92 p.

Hartzell, S., 1989, Comparison of waveform inversion results for the rupture history of a finite fault: Application to the 1986 North Palm Springs, California, earthquake: Journal of Geophysical Research, v. 94, p. 7515–7534.

Hauksson, E., and nine others, 1992, Overview of the 1992 (M 6.1, 7.5, 6.6) Landers earthquake sequence in San Bernardino County, California [abs.]: Eos (Transactions, American Geophysical Union), v. 73, p. 357.

Lees, J.M., 1990, Tomographic *P*-wave velocity images of the Loma Prieta earthquake asperity: Geophysical Research Letters, v. 17, p. 1433–1436.

Lees, J.M., and Crosson, R.S., 1989, Tomographic inversion for three-dimensional velocity structure at Mount St. Helens using earthquake data: Journal of Geophysical Research, v. 94, p. 5716–5728.

Lees, J.M., and Malin, P.E., 1990, Tomographic images of *P*-wave velocity variation at Parkfield, California: Journal of Geophysical Research, v. 95, p. 21,793–21,804.

Lees, J.M., and Shalev, E., 1992, On the stability of *P*-wave tomography at Loma Prieta: A comparison of parameterizations, linear and non-linear inversions: Seismological Society of America Bulletin, v. 82, p. 1821–1839.

Lees, J.M., and Vandecar, J.C., 1991, Seismic tomography constrained by Bouguer gravity anomalies: Applications in western Washington: Pure and Applied Geophysics, v. 135, p. 31–52.

Michael, A.J., and Eberhart-Phillips, D., 1991, Relations among fault behavior, subsurface geology, and three-dimensional velocity models: Science, v. 253, p. 651–654.

Nicholson, C., and Hauksson, E., 1992, The April 1992 $M_L$ 6.1 Joshua Tree earthquake sequence: Seismotectonic analysis and implications [abs.]: Eos (Transactions, American Geophysical Union), v. 73, p. 363.

Nicholson, C., and Lees, J.M., 1992, Travel-time tomography in the northern Coachella Valley using aftershocks of the 1986 $M_L$ 5.9 North Palm Springs earthquake: Geophysical Research Letters, v. 19, p. 1–4.

Rymer, M.J., 1992, The 1992 Joshua Tree, California, earthquake: Tectonic setting and triggered slip [abs.]: Eos (Transactions, American Geophysical Union), v. 73, p. 363.

Scott, J.S., 1992, Microearthquake studies in the Anza seismic gap [Ph.D. thesis]: San Diego, University of California, p. 277.

Wald, D., Helmberger, D.V., Thio, H.K., Dreger, D., and Heaton, T.H., 1992, On developing a single rupture model for the 1992 Landers, California, earthquake consistent with static, broadband teleseismic, regional and strong motion data sets [abs.]: Eos (Transactions, American Geophysical Union), v. 73, p. 358.

Young, R.P., and Maxwell, S.C., 1992, Seismic characterization of a highly stressed rock mass using tomographic imaging and induced seismicity: Journal of Geophysical Research, v. 97, p. 12,361–12,374.



Manuscript received January 7, 1993
Revised manuscript received February 10, 1993
Manuscript accepted February 18, 1993